

Hierarchical Characterization of Thermoelectric Performance in Copper-Based Chalcogenide CsCu_3S_2 : Unveiling the role of Anharmonic Lattice Dynamics

Jincheng Yue,^{†,‡} Junda Li,^{†,‡} Jiongzhi Zheng,^{*,¶,§,‡} Xingchen Shen,^{||} Wenling Ren,[⊥] Geoffroy Hautier,[¶] Yanhui Liu,^{*,†} and Tian Cui^{*,†,#}

[†]*Institute of High Pressure Physics, School of Physical Science and Technology, Ningbo University, Ningbo, 315211, China*

[‡]*These authors contributed equally*

[¶]*Thayer School of Engineering, Dartmouth College, Hanover, New Hampshire, 03755, USA*

[§]*Department of Mechanical and Aerospace Engineering, The Hong Kong University of Science and Technology, Clear Water Bay, Kowloon, 999077, Hong Kong*

^{||}*Laboratoire de Cristallographie et Sciences des Matériaux (CRISMAT), CNRS, ENSICAEN, Caen, 14000, France*

[⊥]*Institute of Materials Science, Technical University of Darmstadt, Darmstadt, 64287, Germany*

[#]*State Key Laboratory of Superhard Materials, College of Physics, Jilin University, Changchun, 130012, China*

Keywords: thermoelectric material, Cu-based chalcogenide, lattice anharmonicity, wigner transport equation, self-consistent phonon theory

E-mail: jiongzhi.zheng@dartmouth.edu; liuyanhui@nbu.edu.cn; cuitian@nbu.edu.cn

Abstract

Fundamental understanding of anharmonic lattice dynamics and heat conductance physics in crystalline compounds is critical for the development of thermoelectric energy conversion devices. Herein, we thoroughly investigate the microscopic mechanisms of thermal transport in CsCu_3S_2 by coupling the self-consistent phonon (SCP) theory with the linearized Wigner transport equation (LWTE). We explicitly consider both phonon energy shifts and broadening arising from both cubic and quartic anharmonicities, as well as diagonal/non-diagonal terms of heat flux operators in thermal conductivity. Our findings show that the strong anharmonicity of CsCu_3S_2 primarily arises from the presence of p - d anti-bonding hybridization between Cu and S atoms, coupled with the random oscillations of Cs atoms. Notably, the competition between phonon hardening described by the loop diagram and softening induced by the bubble diagram significantly influences particle-like propagation, predominantly reflected in group velocity and energy-conservation rule. Additionally, the electrical transport properties are determined by employing the precise momentum relaxation-time approximation (MRTA). At high temperatures, the thermoelectric performance of p -type CsCu_3S_2 reaches its optimum theoretical value of 0.94 along the in-plane direction based on advanced phonon renormalization theory. In striking contrast, the harmonic approximation theory significantly overestimates the thermoelectric efficiency at the same temperatures, rendering it an impractical expectation. Conversely, the first-order renormalization approach leads to a serious underestimation of the thermoelectric properties due to the over-correction of phonon energy. Our study not only reveals the pivotal role of anharmonic lattice dynamics in accurately assessing thermoelectric properties but also underscores the potential thermoelectric applications for novel copper-based chalcogenides.

Introduction

Thermoelectric materials with low costs and superior performance are currently undergoing extensive research due to their potential for widespread application in waste heat recovery across manufacturing, processing, and automotive sectors.^{1–3} The figure of merit ZT is commonly used to assess the conversion efficiency of thermoelectric materials, $ZT=S^2\sigma/\kappa$, where S and σ represents the Seebeck coefficient and conductivity respectively; κ consists of electronic thermal conductivity (κ_e) and lattice thermal conductivity (κ_L).^{4–6} Given the challenges of decoupling electron transport parameters, achieving intrinsic ultra-low κ_L has emerged as a prerequisite for attaining high thermoelectric properties.^{7–9} Within the framework of theoretical calculations, numerous promising thermoelectric materials have been reported in recent years owing to their exceptionally low κ_L at room temperature; e.g., chalcogenide AgIn_5S_8 (0.97 W/mK),¹⁰ BaTiS_3 (0.25 W/mK)¹¹ $\text{Cu}_2\text{AgBiPbS}_4$ (0.3 W/mK),¹² oxide LaZnOPn (Pn = P, As) (2 W/mK),¹³ BaBi_2O_6 (3.6 W/mK),¹⁴ layered intermetallic Na_2MgSn (0.81 W/mK),¹⁵ full-Heusler Li_2TiBi (2.36 W/mK)¹⁶ and alkali-based telluride BaIn_2Te_4 (1 W/mK).¹⁷ In essence, the ultra-low κ_L often correlates with strong lattice anharmonicity, which is commonly induced by distinctive electron/atomic configurations, including the lone electron pairs,¹⁸ resonant bonding,¹⁹ host-guest structures,^{20,21} and so on.

Recent advancements in thermoelectric materials underscore the potential of copper-based chalcogenides as highly promising candidates for thermoelectric applications.^{22,23} Compared to conventional thermoelectric materials, copper-based chalcogenides offer numerous advantages, including inherent non-toxic properties, cost-effectiveness, and environmental friendliness. For example, superionic conductor (SIC), e.g., $\text{Cu}_2\text{Se}_{1-x}\text{S}_x$,²⁴ exhibits ultra-low κ_L of $< 1 \text{ W m}^{-1}\text{ K}^{-1}$ attributed to that the disordered arrangement of atoms induced by the liquid-like sublattice enhances the scattering rates of main heat carriers. However, the liquid-like migration behavior tends to degrade the performance of thermoelectric devices and shorten their lifetimes. Importantly, the introduction of ionic alkali metals has been proven to limit the occurrence of the superionic phase.^{22,25} Previously, Hirohiko et al.²⁶ successfully synthesized ternary copper-based alkali metal chalcogenides CsCu_3S_2 . Their experimental results confirmed the thermodynamic stability of CsCu_3S_2

and revealed a significant decrease in resistivity after soaking in an ammonium solution. Additionally, Li et al. proposed a valid empirical descriptor based on high-throughput screening to predict a series of crystals with ultra-low κ_L ($< 2 \text{ Wm}^{-1}\text{K}^{-1}$), including the CsCu_3S_2 .²⁷ Nevertheless, the predictive models based on the harmonic approximation (HA) treatment faces challenges in predicting thermal conductivity when applied to highly anharmonic crystals because they remarkably underestimated the phonon energy.^{28,29} Meanwhile, the temperature effect on particle-like propagation properties is solely reflected in the Bose-Einstein distribution of phonons.³⁰

In highly anharmonic crystalline compounds, the thermal or quantum fluctuations of atoms are too large for quasiharmonic phonon theory to accurately evaluate lattice dynamics.³¹ Concurrently, the lattice dynamics is pivotal in defining key thermal transport properties, such as phonon velocities and rates of anharmonic scattering.^{32,33} These factors are crucial in determining thermal conductivity and its dependency on temperature, as they govern the patterns of phonon transport and interaction within the crystal framework.^{34,35} With the development of the phonon self-consistency theory based on the quasiparticle (QP) approximation, the effective one-body Hamiltonian of interacting phonons has been achieved to capture the accurate modeling of anharmonic lattice dynamics at finite temperatures.^{31,36} However, explicitly considering both cubic and quartic anharmonicities in phonon energy shifts and phonon scattering rates is still lacking in the study of thermal transport and figure of merit in copper-based chalcogenides, as well as in most other thermoelectric materials.^{37,38} Furthermore, a unified theory of thermal transport proposed by Simoncelli et al. enables the integration of the off-diagonal elements of heat-flux operators, enriching the computational framework including accurately depicting wavelike heat conduction.^{39,40} A comprehensive investigation aimed at accurately describing thermal transport and figure of merit is not only fundamentally interesting but also paves the way to better understand and engineer the thermoelectric performance of known compounds.

In this work, we have systematically investigated the effect of the anharmonic lattice dynamics on the thermoelectric properties of copper-based chalcogenides CsCu_3S_2 at the atomic level. Considering that reliable modeling of lattice dynamics requires accurate treatment of lattice an-

harmonicity, our calculation involves second-order anharmonic self-energy Feynman diagrams. Significantly, the net frequency shift of phonon frequencies induced by third- and fourth-order anharmonicity exerts a decisive influence on thermoelectric properties. Using the unified heat transport equation which includes particle-like propagation and wave-like tunneling channels, the thermoelectric properties of *p*-type CsCu₃S₂ are estimated accurately, and the optimal theoretical value of 0.94 is obtained along the in-plane direction at 900 K. By contrast, the predicted thermoelectric value using the traditional harmonic approximation treatment is overestimated by 88%, reaching an unrealistic expected value of 1.77. Conversely, only considering the first-order renormalization contribution approach underestimates the thermoelectric properties by about 15% because of the over-correction of phonon energy. Our research highlights the pivotal influence of anharmonic lattice dynamics on accurately assessing thermoelectric properties, underscoring the necessity to understand intricate lattice dynamics for effective thermoelectric energy conversion.

Methodology

All the density functional theory (DFT) calculations were performed using the projected Enhanced wave (PAW) method and implemented in the Vienna Ab initio Simulation Package.^{41–43} The exchange-correlation function adopted the Perdew-Burke-Ernzerhof (PBE) function within the generalized gradient approximation; meanwhile, the optB86b-vdW was employed to accurately describe the van der Waals (vdW) interactions.^{44,45} A kinetic energy cutt-off of 600 eV, coupled with a 20×20×20 Monkhorst-Pack *k*-point mesh, was adopted to ensure enough sampling of the Brillouin zone for the primitive cell. The energy and force-convergence criteria of 10^{−8} eV and 10^{−6} eV·Å^{−1} were used for both the structural optimization and statical self-consistent DFT calculation, respectively.

In terms of assessing the zero-K harmonic force constants (IFCs), the finite-displacement method was meticulously applied.⁴⁶ The static DFT calculations were conducted on a robust 3×3×2 supercell containing 108 atoms and using a 4×4×4 *k*-point mesh. To train the higher-order

anharmonic IFCs, a comprehensive dataset comprising 200 atomic configurations was employed. A displacement magnitude of 0.15 Å was systematically applied to each atom in randomly selected vectors to diminish structural cross-correlations, facilitated by a random-seed algorithm.^{47,48} The compressive sensing lattice dynamics (CSLD) framework, alongside the discerning least absolute shrinkage and selection operator (LASSO) methodology, was harnessed to filter and affirm the physically important terms of IFCs, as integrated within the ALAMODE package.⁴⁹

After obtaining the harmonic and anharmonic IFCs, the anharmonic phonon energy renormalization was carried out by applying the self-consistent phonon theory in the reciprocal space.⁵⁰ Assuming only the first-order perturbation due to the quartic anharmonicity, namely the loop diagram, the first-order self-consistent phonon (SC1) equation can be derived in the diagonal form as follows:³⁰

$$\Omega_q^2 = \omega_q^2 + 2\Omega_q I_q \quad (1)$$

$$I_q = \frac{1}{8N} \sum_{q'} \frac{\hbar\Phi(q; -q; q'; -q')}{4\Omega_q \Omega_{q'}} [1 + 2n(\Omega_{q'})] \quad (2)$$

where ω_q^2 is the bare harmonic phonon frequency associated with the phonon mode q , and Ω_q^2 is the anharmonically renormalized phonon frequency at finite temperatures. The n and $\Phi(q; -q; q'; -q')$ represent the Bose-Einstein distribution ($n(\omega) = 1/[\exp(\hbar\omega/k_B T) - 1]$), and the reciprocal representation of 4th-order IFCs, respectively. Within the framework of QP approximation and utilizing phonon energies renormalized by loop diagram, the additional negative frequency shifts ascribing from the bubble self-energy can be estimated by the following self-consistent equation:³¹

$$(\Omega_q^B)^2 = \Omega_q^2 - 2\Omega_q \text{Re} \sum_B^q [G, \Phi_3](\Omega = \Omega_q^B) \quad (3)$$

where $\sum_B^q [G, \Phi_3]$, B , and Φ_3 denote the frequency-dependent bubble self-energy, bubble diagram, and third-order force constant, respectively. Noteworthily, the nonlinear treatment option (QPNL) was chosen to solve Eq. (3) and obtain the fully renormalized phonon energies that account for cubic and quartic anharmonicities.

Within the linearized Wigner transport equation (LWTE) framework, the thermal conductivity $\kappa_L^{P/C}$ can be described as:³⁹

$$\begin{aligned}\kappa_L^{P/C} = & \frac{\hbar^2}{k_B T^2 V N_0} \sum_q \sum_{j,j'} \frac{\Omega_{qj} + \Omega_{qj'}}{2} v_{qj'j} \otimes v_{qj'j'} \\ & \times \frac{\Omega_{qj} n_{qj} (n_{qj} + 1) + \Omega_{qj'} n_{qj'} (n_{qj'} + 1)}{4(\Omega_{qj} - \Omega_{qj'})^2 + (\Gamma_{qj} + \Gamma_{qj'})^2} (\Gamma_{qj} + \Gamma_{qj'})\end{aligned}\quad (4)$$

where the V and N_0 denote the primitive-cell volume and number of sampled, respectively. The Γ_q stands for the scattering rates including three-phonon (3ph), four-phonon (4ph), and isotope-phonon scattering processes. The phonon group velocity v_q is extended to encompass off-diagonal components:⁴⁰

$$v_{qj'j} = \frac{\left\langle e_{qj} \left| \frac{\partial D(q)}{\partial q} \right| e_{qj'} \right\rangle}{2 \sqrt{\Omega_{qj} \Omega_{qj'}}} \quad (5)$$

in which the $D(q)$ and e_q are the dynamical matrix and polarization vector, respectively. The particle-like phonon thermal transport properties are computed by using the ShengBTE and Four-Phonon packages, while the wave-like tunneling of phonon channels is evaluated using our in-house code.^{51,52}

The related electronic transport was performed using the AMSET code, wherein the differential scattering rate from the initial ψ_{nk} to final states ψ_{mk+q} for inelastic and elastic processes was calculated as:⁵³

$$\begin{aligned}\tau_{nk \rightarrow mk+q}^{-1} = & \frac{2\pi}{\hbar} |g_{nm}(k, q)|^2 \\ & \times [(n_{po} + 1 - f_{mk+q}) \delta(\epsilon_{nk} - \epsilon_{mk+q} - \hbar\omega_{po}) \\ & + (n_{po} + f_{mk+q}) \delta(\epsilon_{nk} - \epsilon_{mk+q} + \hbar\omega_{po})]\end{aligned}\quad (6)$$

$$\tilde{\tau}_{nk \rightarrow mk+q}^{-1} = \frac{2\pi}{\hbar} |g_{nm}(k, q)|^2 \delta(\epsilon_{nk} - \epsilon_{mk+q}) \quad (7)$$

where ϵ_{nk} symbolizes the specific energy state ψ_{nk} . The $g_{nm}(k, q)$ accounts for three kinds of electron-phonon scattering matrix elements including acoustic deformation potential (ADP), polar optical phonon (POP), and ionized impurity (IMP) matrix element. Notably, the overall elastic

rates were calculated using the momentum relaxation time approximation (MRTA), given by:⁵⁴

$$\tilde{\tau}_{nk}^{-1} = \sum_m \int \frac{d}{\Omega_{BZ}} [1 - \frac{\mathbf{v}_{nk} \cdot \mathbf{v}_{mk+q}}{|\mathbf{v}_{nk}|^2} \tilde{\tau}_{nk \rightarrow mk+q}^{-1}] \quad (8)$$

Results and Discussion

The CsCu₃S₂ crystallizes in the trigonal space group *P*[−]*3m1* (No. 164), in which the corresponding Wyckoff positions of Cs, Cu, and S atoms are 1b, 3e, and 2d sites, respectively. The configurations of CsCu₃S₂ are originated from the [Cu₃S₂][−] pyramidal-like structural motif and independent Cs⁺ ions. These [Cu₃S₂][−] units pass through two opposite sides with two-coordinated Cu atoms to form a wave layer and propagate periodically along with the in-plane direction; meanwhile, they are interlaced with Cs⁺ ion layers and piled up along with the out-of-plane direction, as shown in Figures 1(a-b). According to the charge density equipotential surface, the overlapping charge density is mainly distributed between Cu and S atoms, while the valence electron cloud of the Cs⁺ ions is confined to its nucleus surface. Additionally, the predominant distribution of overlapping charge densities is observed within the layers of [Cu₃S₂][−], indicating that the bonding character between Cu and S atoms exhibits a pronounced inclination towards covalent interactions. In contrast, the valence electrons of the Cs⁺ ions are predominantly localized at the periphery of the atomic nucleus, suggesting that the electrostatic interaction between Cs⁺ ions and [Cu₃S₂][−] structures is relatively weak.

Uncovering the weak interatomic interaction can be done intuitively through noncovalent (NCL) interaction analysis.⁵⁵ The NCI index can be effectively quantified using the Interaction Region Indicator (IRI), which operates as a function characterized by sign(λ_2) ρ .⁵⁶ In this expression, ρ denotes the electron density, while sign(λ_2) reflects the sign associated with the second eigenvalue in the electron density Hessian matrix. Within regions characterized by diminished electron density ($|\text{sign}(\lambda_2)\rho| < 0.01$ a.u.), the weak interaction is typically delineated by salient peaks, which signal significant alterations in the relative differential gradient (RDG) as it approaches

the zero threshold at the critical point, as demonstrated by Figure 1(c). Simultaneously, the three-dimensional IRI isosurfaces, highlighted by BGR color bars, demonstrate that the weak vdW forces are primarily localized around the Cs^+ ions. As a result, the Cs^+ ions display stochastic oscillation behavior similar to rattles, accompanied by larger mean squared atomic displacements (MSDs). [see Figure S1] In Figure 1(d), we conducted a detailed examination of the orbital-resolved partial density of states (PDOS) and crystal orbital Hamiltonian populations (COHP) to elucidate the characteristics of the Cu-S bonding interactions. The Cu(d)-orbitals converge energetically with the S(p)-orbitals, fostering a robust p - d hybridization with a wide energy range.^{57,58} Such strong hybridization propels the occupied antibonding states up to the Fermi level, diminishing the bond strength and manifesting metavalent-like bonding characteristics.⁵⁹ On the whole, the hybridization of p - d antibonding orbitals between Cu and S atoms, in conjunction with the stochastic vibrations of Cs^+ ions, gives rise to potentially strong lattice anharmonicity.²³

Figure 2(a) shows the anharmonically renormalized phonon dispersions at a finite temperature in comparison with those obtained from harmonic approximation. Obviously, the acoustic and mid-frequency optical branches ($< 180 \text{ cm}^{-1}$) undergo a notable hardening, whereas the high-frequency optical branches exhibit a non-negligible softening as temperature increases. It is essential to note the significance of both cubic and quartic interatomic force constants in accurately predicting the lattice dynamics within materials exhibiting strong anharmonicity. In general, the frequency shift caused by anharmonicity at a finite temperature is represented by the real part of the phonon self-energy.^{21,30} Specifically, considering the first-order corrections arising from fourth-order anharmonicity (SCPH), the SCPH method typically generates a positive contribution to the phonon frequency. Nevertheless, the SCPH theory tends to overestimate phonon frequencies, a tendency predominantly because of the neglection of the negative frequency shift associated with bubble self-energy.^{28,31} Subsequently, we compare the temperature-dependent phonon frequency difference of TO_{5th} mode at Γ point, including the loop diagram with the polarization mixing (PM), and that of the bubble diagram respectively. [see Figure S2] Indeed, the observed negative shift is considerable in the highly anharmonic CsCu_3S_2 , which exerts an essential effect on the theoretical

prediction of phonon linewidth and consequent thermoelectric properties, as we discuss later.

Besides, we further delve deeper to uncover the fundamental characteristics of its lattice dynamics. Along the G-M direction, an evident avoided-crossing interaction is discernible between the longitudinal acoustic (LA) branches and low-lying optical (LLO) branches, which leads to a substantial influence on the heat-carrying phonon transport within this region.⁶⁰ To begin with, the presence of the avoided-crossing point is expected to suppress the group velocity around the LA branch, akin to observations from the inelastic neutron scattering analysis of Ba₈Ga₁₆Ge₃₀.^{37,49} The LA branch, which is initially the most heavily colored, is noticeably lightened after passing through the crossing point. [see Figure S3] Additionally, there is a marked hybridization between the optical and acoustic vibrational states near the avoided-crossing point, meaning strong coupling of these phonon modes. By hybridizing the optical phonon eigenvectors into acoustic phonons, the scattering rates of the LA branch increase by several orders of magnitude, even at low-frequency limits.⁶¹ On the other hand, the atomic participation ratio (APR) serves as a quantitative degree to assess the involvement of atoms in a specific phonon mode,

$$APR_{qj,i} = \frac{|e(i; qj)|^2}{M_i} / \left(N \sum_{i=1}^N \frac{|e(i; qj)|^4}{M_i^2} \right)^{1/2} \quad (9)$$

where the e , i , M , and N represent phonon eigenvector, atomic index, atomic mass, and total number of atoms, respectively. In Figures 2(b-e), it is observed that the low-energy Einstein optical modes participating in the eigenvector hybridization, predominantly originate from the oscillations of Cs⁺ ions. Numerous flattened low-energy optical branches remarkably assist in the scattering of acoustic phonons responsible for heat transport.⁶² By contrast, the Cu atoms predominantly contribute to the acoustic phonons and mid-frequency optical phonons, whereas the S atom exerts a dominant influence over the high-frequency optical phonon modes.

Afterwards, the investigation delves into the influence of anharmonic lattice dynamics on the thermal conductivity κ_L within the CsCu₃S₂ crystal, as presented in Figure 3(a). For particle-like propagation, the lattice thermal conductivities κ_L^P obtained from the HA+3,4ph model, are

1.24 and $0.88 \text{ Wm}^{-1}\text{K}^{-1}$, respectively. Remarkably, the thermal energy is constrained within the $[\text{Cu}_3\text{S}_2]^-$ layers owing to the "quasi-stationary" nature of Cs^+ ions [see Figure 2(b)], facilitating its directional transport primarily along the in-plane direction (x -axis).⁶³ After considering the first-order correction of the fourth-order anharmonicity to the dynamic matrix, namely, the SCPH+3,4ph model, the predicted κ_L^P reaches 2.20 and $1.65 \text{ Wm}^{-1}\text{K}^{-1}$. We attribute this to the marked enhancement in the phonon group velocities coupled with a prolonged phonon relaxation time. [see Figure 3(b)] Incorporating the effects of third-order anharmonicity, namely, the SCPB+3,4ph model, the negative frequency shift further leads to the decrease of thermal conductivity, with the values descending to 1.80 and $1.37 \text{ Wm}^{-1}\text{K}^{-1}$, respectively. Correspondingly, both the group velocity and phonon relaxation time exhibit an analogous trend in variation, underscoring the consistent nature of their respective evolutions within the framework of the dynamics. Significantly, the determinants of phonon lifetime under diverse theories are exclusively determined by the strict energy conservation laws.⁶⁴ As illustrated in Figures 3(c-d), the Peierls's thermal conductivity κ_L^P is almost entirely contributed by phonons below 100 cm^{-1} . Meanwhile, it also reveals that the competitive relationship between phonon hardening described by the loop diagram and softening induced by the bubble diagram has a decisive influence on particle propagation.²⁸

Temperature-dependent fluctuations in thermal conductivity κ_L^P can be attributed to anharmonic lattice dynamics as well. As anticipated, considering the 3,4ph scattering process in conjunction with the zero-K second-order force constant, derived from the HA+3,4ph model, the κ_L^P follows the temperature dependence of $T^{-1.37/-1.34}$. Such a trend diverges from the conventional T^{-1} relationship as the introduction of additional 4ph scattering tends to enhance the temperature-dependence of κ_L^P .^{35,65} [see Figure S4] The SCPH+3,4ph method using first-order renormalization drastically weakens the temperature dependence of thermal conductivity to $T^{-0.86/-0.78}$. In contrast to the SCPH+3,4ph model, the SCPB+3,4ph model gives rise to a faster decay of $T^{-1.05/-1.07}$ via further including the negative frequency shift. It is essential to underscore that while the temperature dependence exhibited under the SCPB+3,4ph model aligns with the outcomes of the lowest-order theoretical HA+3ph model, the anharmonic lattice dynamics still have an irreplaceable role in

accurately predicting the thermal conductivity.

Traditionally, in Peierls-Boltzmann transport theory, coherence terms—specifically, the off-diagonal elements of heat flux operators—are disregarded, a valid assumption when phonon inter-branch spacings significantly exceed linewidths.^{39,40} Nonetheless, as the phonon mean free path (MFP) nears the interatomic spacing, these off-diagonal contributions become non-negligible and amenable to calculation through a unified framework of thermal transport.²⁸ [see Figure 3(a) and Eq.(4)] Generally, phonons with a lifetime below the Wigner time limit $[\Delta\omega_{av}]^{-1}$ (red solid line in Figure 3(b)), mainly contribute to coherence conductivity κ_L^C via wave-like tunneling. [see Figure 3(b)] As indicated by Figures 4(a-d), the coherence conductivity κ_L^C primarily originates from the quasi-coalescing vibrations ($\omega_{qj} \cong \omega_{qj}$) within the low- to intermediate-frequency region (< 180 cm⁻¹). In particular, flat low-energy optical branch (50-100 cm⁻¹) primarily driven by the Cu⁺ and rattling-like Cs⁺ ions are correlated with strong 4ph scattering, which tends to inhibit particle-like thermal transport and promotes coherence among non-degenerate states.³² [see Figure 2(c-d)] On the contrary, high-frequency optical phonons generate negligible influence on both particle-like propagation and wave-like tunneling, primarily due to their extremely flat dispersion characteristics. [see Figures 3(b-f) and Figure 2(b)]

The theoretically predicted ultra-low thermal conductivity κ_L of CsCu₃S₂ underscores its prospects for integration into thermoelectric devices. Consequently, we thoroughly investigate its electron structure and transport properties within the framework of the momentum relaxation time approximation (MRTA).⁵³ As mentioned earlier, the hybridization of Cu(*d*)-S(*p*) orbitals produces an antibonding state below the Fermi level, which also determines the band structure and electron transport properties.^{23,59} [see Figure 1(d)] Our computation reveals an indirect band gap quantified at 1.6 eV using PBE (HSE06: 2.6 eV), positioning the valence band maximum (VBM) at the A point, accompanied by a double degeneracy. [see Figure 5(a)] The integration of dual-band transmission with the spatial multi-valley convergence at point A facilitates the enhancement of electrical conductivity and the Seebeck coefficient, thereby guaranteeing that both parameters are optimized and intended for improving thermoelectric performance.^{66,67} [see Figure 5(b)]

Moreover, the specific type of doping is a priority when thermoelectric materials are synthesized industrially, while the likelihood of *p*-type or *n*-type doping can be inferred from the ionization potentials (IP) and electron affinity (EA).⁶⁸ Generally, the lower IP implies that the low ionization potentials from high-lying valence band maxima drive semiconducting materials to produce holes.⁶⁹ The vacuum and core energies were used to compute the band alignment for two materials according to the core-vacuum alignment scheme.

$$IP = (E_{vac} - E_{core,slab}) - (E_{VBM} - E_{core,bulk}) \quad (10)$$

where the E_{vac} presents the energies of the vacuum and the $E_{core,slab}$ denotes the core level in the bulk-like surface slab. The E_{VBM} and $E_{core,bulk}$ are the valence band maximum and core energy of the bulk, respectively. The Cu 2*p* state was used for aligning the energy levels, which has been widely used in previous copper-based chalcogenide (CBC) compounds, and the (001) slab was utilized to obtain the energies of the surface.⁷⁰ As demonstrated in Figure 5(c), the calculated IP of CsCu₃S₂ with 3.6 eV, aligns with that of conventional *p*-type semiconductors such as LaZnOAs (3.6 eV), and LaZnOP (3.9 eV).¹³ Accordingly, its low-lying IP is indicative of a propensity for hole doping, which demonstrates its considerable promise as a *p*-type thermoelectric material.

Figures 6(a-f) present a comprehensive depiction of the thermal variation in electron properties such as electrical conductivity σ , Seebeck coefficient S , and electronic thermal conductivity κ_e for CsCu₃S₂ ranging from 10¹⁸ to 10²¹ cm⁻³ and temperatures spanning from 300 to 900 K. The VBM is chiefly characterized by the orbital intermingling of Cu and S atoms, resulting in conductance being predominantly conveyed across the in-plane within the [Cu₃S₂]⁻ layers, as evidenced by the carrier mobility. [see Figure S5] Within the carrier scattering mechanisms, the dominance of inelastic interactions associated with polar optical phonons constitutes a significant impediment to carrier mobility. [see Figure S6] The observed conductivity σ exhibits an inverse relationship with temperature while maintaining a direct proportionality with the carrier concentration. Similarly, the electronic thermal conductivity κ_e parallels the conductivity σ in its correlation with

temperature and carrier concentration, a relationship that is consistent with the principles of the Wiedemann-Franz law.⁷¹ On the contrary, the Seebeck coefficient S is determined by the ratio of the first moment of the generalized transport coefficient to the conductivity σ , thereby exhibiting an inverse dependency on both temperature and carrier concentration.⁷² In situations of strong electrical transport parameter coupling, the power factor $S^2\sigma$ is predicted to reach its maximum value of $1.25 \text{ mWm}^{-1}\text{K}^{-1}$ along with the in-plane direction at 900 K and the carrier concentration of 10^{21} cm^{-3} .

Subsequently, our investigation explores the influences that anharmonic lattice dynamics exert on the thermoelectric properties, as exemplified by Figure 7(a-f). Under the carrier concentration of $1.49 \times 10^{20} \text{ cm}^{-3}$ and temperature of 900 K, the HA+3,4ph model, gives a theoretical maximum of 1.77 along with the in-plane direction. Such impressive value even qualifies this material as a high-caliber candidate in the realm of thermoelectric materials. However, the first-order SCPH+3,4ph theory indicates that the optimal value is only 0.8, corresponding to a carrier concentration of $3.04 \times 10^{20} \text{ cm}^{-3}$ at the same temperature. The overcorrection of the fourth-order anharmonicity on phonon energies is chiefly responsible for the virtual high of thermal conductivity κ_L and the consequent underperformance in thermoelectric properties. Further, the second-order SCPB+3,4ph model combined with the OD term further improves the optimal ZT values to 0.94 with a carrier of $2.4 \times 10^{20} \text{ cm}^{-3}$. Emphatically, although the ZT values derived from the SCPB+3,4ph+OD model may not be particularly remarkable, they are physically correct. In particular, the incorporation of sufficient anharmonic lattice dynamics is crucial for precisely determining the optimal thermoelectric properties and doping levels, thereby advancing the experimental exploration of thermoelectric materials with strong anharmonicity.

Conclusions

In conclusion, we have systematically investigated the influences of anharmonic lattice dynamics on the thermoelectric properties within the crystalline CsCu_3S_2 . Initially, our findings demonstrate

that the strong anharmonicity of the CsCu_3S_2 is driven by the p - d antibonding hybridization occurring between the Cu and S atoms and the stochastic vibrations of Cs ions. Subsequently, we compare the lattice dynamics within HA, first-order SCPH, and second-order SCPB frameworks, examining the particle-like thermal conduction considering three- and four-phonon scattering. Especially, it is discovered that the anharmonic renormalization, stemming from both cubic and quartic anharmonicities, plays a vital role in the accurate depiction of thermal transport. The competition between the loop diagram and bubble diagram for phonon energy determines the particle-like group velocity and energy conservation rules, which indirectly affect the thermoelectric properties. Furthermore, the low ionization potentials within the CsCu_3S_2 render it more amenable to p -type doping following the establishment of band alignment. The traditional HA+3,4ph theory tends to considerably overestimate the thermoelectric efficiency, reaching 1.77 along with in-plane direction at 900 K, which results in setting impractical expectations. Conversely, the overcorrection of phonon self-energy by the one-order SCPH+3,4ph model results in a serious underestimation of the thermoelectric properties. In contrast, by employing the advanced renormalization theory, the second-order SCPB+3,4ph in conjunction with the OD term, we can derive thermal conductivity that is physically plausible, alongside the related thermoelectric characteristics. At 900 K, the thermoelectric properties of p -type CsCu_3S_2 reach its optimum theoretical value of 0.94 along the in-plane direction. Our research highlights the pivotal influence of anharmonic lattice dynamics on the precise assessment of thermoelectric characteristics, providing a reliable framework for experimental investigations into the thermoelectric behavior of highly anharmonic crystals.

Author Contributions

The authors confirm their contribution to the paper as follows: writing - original draft : J.C.Y. and J.Z.Z.; conceptualization : J.D.L; data curation : J.C.Y. and W.L.R; investigation: X.C.S; writing - review & editing : Y.H.L and T.C.; funding acquisition : T.C. All authors reviewed the results and approved the final version of the manuscript.

Conflicts of interest

The authors declare that they have no known competing financial interests or personal relationships that could have appeared to influence the work reported in this paper

Acknowledgement

This work was supported by the National Natural Science Foundation of China (Grant No. 52072188, No. 12204254), the Program for Science and Technology Innovation Team in Zhejiang (Grant No. 2021R01004), and the Natural Science Foundation of Zhejiang province (Grant No. LQ23A040005). We are grateful to the Institute of High-pressure Physics of Ningbo University for its computational resources.

References

- (1) Yin, L.; Yang, F.; Bao, X.; Xue, W.; Du, Z.; Wang, X.; Cheng, J.; Ji, H.; Sui, J.; Liu, X.; others Low-temperature sintering of Ag nanoparticles for high-performance thermoelectric module design. *Nat. Energy* **2023**, *8*, 665–674.
- (2) Liu, D.; Wang, D.; Hong, T.; Wang, Z.; Wang, Y.; Qin, Y.; Su, L.; Yang, T.; Gao, X.; Ge, Z.; others Lattice plainification advances highly effective SnSe crystalline thermoelectrics. *Science* **2023**, *380*, 841–846.
- (3) Kimber, S. A.; Zhang, J.; Liang, C. H.; Guzmán-Verri, G. G.; Littlewood, P. B.; Cheng, Y.; Abernathy, D. L.; Hudspeth, J. M.; Luo, Z.-Z.; Kanatzidis, M. G.; others Dynamic crystallography reveals spontaneous anisotropy in cubic GeTe. *Nat. Mater.* **2023**, *22*, 311–315.
- (4) Dong, J.; Suwardi, A.; Tan, X. Y.; Jia, N.; Saglik, K.; Ji, R.; Wang, X.; Zhu, Q.; Xu, J.; Yan, Q. Challenges and opportunities in low-dimensional thermoelectric nanomaterials. *Mater. Today* **2023**,

- (5) He, J.; Amsler, M.; Xia, Y.; Naghavi, S. S.; Hegde, V. I.; Hao, S.; Goedecker, S.; Ozoliņš, V.; Wolverton, C. Ultralow thermal conductivity in full Heusler semiconductors. *Phys. Rev. Lett.* **2016**, *117*, 046602.
- (6) Yue, J.; Guo, S.; Li, J.; Zhao, J.; Shen, C.; Zhang, H.; Liu, Y.; Cui, T. Pressure-induced remarkable four-phonon interaction and enhanced thermoelectric conversion efficiency in CuInTe₂. *Mater. Today Phys.* **2023**, *39*, 101283.
- (7) Yue, J.; Zhang, A.; Li, J.; Liu, Y.; Cui, T. Significantly reinforced thermoelectric performance in the novel 1T-Au₆Se₂ monolayer. *APL Mater.* **2023**, *11*.
- (8) Hong, T.; Guo, C.; Qin, B.; Zhang, X.; Gao, X.; Zhao, L.-D. Realizing ultrahigh room-temperature seebeck coefficient and thermoelectric properties in SnTe-based alloys through carrier modulation and band convergence. *Acta Mater.* **2023**, *261*, 119412.
- (9) Yue, J.; Liu, Y.; Ren, W.; Lin, S.; Shen, C.; Singh, H. K.; Cui, T.; Tadano, T.; Zhang, H. Role of atypical temperature-responsive lattice thermal transport on the thermoelectric properties of antiperovskites Mg₃XN (X= P, As, Sb, Bi). *Mater. Today Phys.* **2024**, *41*, 101340.
- (10) Juneja, R.; Singh, A. K. Rattling-induced ultralow thermal conductivity leading to exceptional thermoelectric performance in AgIn₅S₈. *ACS Appl. Mater.* **2019**, *11*, 33894–33900.
- (11) Paudel, T. R.; Tsymbal, E. Y. Evaluating the thermoelectric properties of BaTiS₃ by density functional theory. *ACS omega* **2020**, *5*, 12385–12390.
- (12) Isaacs, E. B.; Lu, G. M.; Wolverton, C. Inverse design of ultralow lattice thermal conductivity materials via materials database screening of lone pair cation coordination environment. *J. Phys. Chem. Lett.* **2020**, *11*, 5577–5583.
- (13) Einhorn, M.; Williamson, B. A.; Scanlon, D. O. Computational prediction of the thermoelectric performance of LaZnOPn (Pn= P, As). *J. Mater. Chem. A* **2020**, *8*, 7914–7924.

- (14) Spooner, K. B.; Ganose, A. M.; Leung, W. W.; Buckeridge, J.; Williamson, B. A.; Palgrave, R. G.; Scanlon, D. O. BaBi₂O₆: a promising n-type thermoelectric oxide with the PbSb₂O₆ crystal structure. *Chem. Mater.* **2021**, *33*, 7441–7456.
- (15) Wang, C.; Chen, Y.; Yao, S.-H.; Zhou, J. Low lattice thermal conductivity and high thermoelectric figure of merit in Na₂MgSn. *Phys. Rev. B* **2019**, *99*, 024310.
- (16) He, J.; Xia, Y.; Naghavi, S. S.; Ozoliņš, V.; Wolverton, C. Designing chemical analogs to PbTe with intrinsic high band degeneracy and low lattice thermal conductivity. *Nat. Commun.* **2019**, *10*, 719.
- (17) Gürel, T.; Altunay, Y. A.; Bulut, P.; Yıldırım, S.; Sevik, C. Comprehensive investigation of the extremely low lattice thermal conductivity and thermoelectric properties of BaIn₂Te₄. *Phys. Rev. B* **2022**, *106*, 195204.
- (18) Wang, S.; Sun, Y.; Yang, J.; Duan, B.; Wu, L.; Zhang, W.; Yang, J. High thermoelectric performance in Te-free (Bi, Sb)₂Se₃ via structural transition induced band convergence and chemical bond softening. *Energy Environ. Sci.* **2016**, *9*, 3436–3447.
- (19) Delaire, O.; Ma, J.; Marty, K.; May, A. F.; McGuire, M. A.; Du, M.-H.; Singh, D. J.; Podlesnyak, A.; Ehlers, G.; Lumsden, M.; others Giant anharmonic phonon scattering in PbTe. *Nat. Mater.* **2011**, *10*, 614–619.
- (20) Tadano, T.; Tsuneyuki, S. Quartic anharmonicity of rattlers and its effect on lattice thermal conductivity of clathrates from first principles. *Phys. Rev. Lett.* **2018**, *120*, 105901.
- (21) Tadano, T.; Gohda, Y.; Tsuneyuki, S. Impact of rattlers on thermal conductivity of a thermoelectric clathrate: a first-principles study. *Phys. Rev. Lett.* **2015**, *114*, 095501.
- (22) Ma, N.; Li, Y.-Y.; Chen, L.; Wu, L.-M. α -CsCu₅Se₃: discovery of a low-cost bulk selenide with high thermoelectric performance. *J. Am. Chem. Soc.* **2020**, *142*, 5293–5303.

- (23) Yue, J.; Zheng, J.; Li, J.; Guo, S.; Ren, W.; Liu, H.; Liu, Y.; Cui, T. Ultralow Glassy Thermal Conductivity and Controllable, Promising Thermoelectric Properties in Crystalline o- CsCu_5S_3 . *ACS Appl. Mater. Interfaces* **2024**,
- (24) Zhang, Z.; Zhao, K.; Wei, T.-R.; Qiu, P.; Chen, L.; Shi, X. Cu₂Se-Based liquid-like thermoelectric materials: looking back and stepping forward. *Energy Environ. Sci.* **2020**, *13*, 3307–3329.
- (25) Ma, N.; Jia, F.; Xiong, L.; Chen, L.; Li, Y.-Y.; Wu, L.-M. CsCu₅S₃: promising thermoelectric material with enhanced phase transition temperature. *Inorg. Chem.* **2019**, *58*, 1371–1376.
- (26) Sato, H.; Kojima, N. Electronic Properties of Low-Dimensional Ternary Copper Chalcogenides A-Cu-X (A = Na, K, Rb, Cs; X = S, Se). *Phosphorus Sulfur Silicon Relat. Elem.* **1992**, *67*, 361–366.
- (27) Li, J.; Hu, W.; Yang, J. High-throughput screening of rattling-induced ultralow lattice thermal conductivity in semiconductors. *J. Am. Chem. Soc.* **2022**, *144*, 4448–4456.
- (28) Zheng, J.; Shi, D.; Yang, Y.; Lin, C.; Huang, H.; Guo, R.; Huang, B. Anharmonicity-induced phonon hardening and phonon transport enhancement in crystalline perovskite BaZrO₃. *Phys. Rev. B* **2022**, *105*, 224303.
- (29) van Roekeghem, A.; Carrete, J.; Osés, C.; Curtarolo, S.; Mingo, N. High-throughput computation of thermal conductivity of high-temperature solid phases: the case of oxide and fluoride perovskites. *Phys. Rev. X* **2016**, *6*, 041061.
- (30) Tadano, T.; Tsuneyuki, S. Self-consistent phonon calculations of lattice dynamical properties in cubic SrTiO₃ with first-principles anharmonic force constants. *Phys. Rev. B* **2015**, *92*, 054301.
- (31) Tadano, T.; Saidi, W. A. First-principles phonon quasiparticle theory applied to a strongly anharmonic halide perovskite. *Phys. Rev. Lett.* **2022**, *129*, 185901.

- (32) Zheng, J.; Lin, C.; Lin, C.; Hautier, G.; Guo, R.; Huang, B. Unravelling ultralow thermal conductivity in perovskite $\text{Cs}_2\text{AgBiBr}_6$: dominant wave-like phonon tunnelling and strong anharmonicity. *NPJ Comput. Mater.* **2024**, *10*, 30.
- (33) Zheng, J.; Shi, D.; Liu, S.; Yang, Y.; Lin, C.; Chang, Z.; Guo, R.; Huang, B. Effects of high-order anharmonicity on anomalous lattice dynamics and thermal transport in fully filled skutterudite $\text{YbFe}_4\text{Sb}_{12}$. *Phys. Rev. Mater.* **2022**, *6*, 093801.
- (34) Xia, Y.; Hegde, V. I.; Pal, K.; Hua, X.; Gaines, D.; Patel, S.; He, J.; Aykol, M.; Wolverton, C. High-throughput study of lattice thermal conductivity in binary rocksalt and zinc blende compounds including higher-order anharmonicity. *Phys. Rev. X* **2020**, *10*, 041029.
- (35) Xia, Y.; Ozoliņš, V.; Wolverton, C. Microscopic mechanisms of glasslike lattice thermal transport in cubic $\text{Cu}_{12}\text{Sb}_4\text{S}_{13}$ tetrahedrites. *Phys. Rev. Lett.* **2020**, *125*, 085901.
- (36) Ravichandran, N. K.; Broido, D. Unified first-principles theory of thermal properties of insulators. *Phys. Rev. B* **2018**, *98*, 085205.
- (37) Xie, Q.-Y.; Liu, P.-F.; Ma, J.-J.; Wu, L.-M.; Zhang, K.-W.; Wang, B.-T. Microscopic mechanisms of glasslike lattice thermal conductivity in tetragonal $\alpha\text{-CsCu}_5\text{Se}_3$. *Phys. Rev. B* **2023**, *108*, 014302.
- (38) Xia, Y.; Pal, K.; He, J.; Ozoliņš, V.; Wolverton, C. Particlelike phonon propagation dominates ultralow lattice thermal conductivity in crystalline Tl_3VSe_4 . *Phys. Rev. Lett.* **2020**, *124*, 065901.
- (39) Simoncelli, M.; Marzari, N.; Mauri, F. Unified theory of thermal transport in crystals and glasses. *Nat. Phys.* **2019**, *15*, 809–813.
- (40) Simoncelli, M.; Marzari, N.; Mauri, F. Wigner formulation of thermal transport in solids. *Phys. Rev. X* **2022**, *12*, 041011.
- (41) Blöchl, P. E. Projector augmented-wave method. *Phys. Rev. B* **1994**, *50*, 17953.

- (42) Kresse, G.; Furthmüller, J.; Hafner, J. Theory of the crystal structures of selenium and tellurium: the effect of generalized-gradient corrections to the local-density approximation. *Phys. Rev. B* **1994**, *50*, 13181.
- (43) Kresse, G.; Joubert, D. From ultrasoft pseudopotentials to the projector augmented-wave method. *Phys. Rev. B* **1999**, *59*, 1758.
- (44) Klimeš, J.; Bowler, D. R.; Michaelides, A. Van der Waals density functionals applied to solids. *Phys. Rev. B* **2011**, *83*, 195131.
- (45) Perdew, J. P.; Burke, K.; Ernzerhof, M. Generalized gradient approximation made simple. *Phys. Rev. Lett.* **1996**, *77*, 3865.
- (46) Esfarjani, K.; Stokes, H. T. Method to extract anharmonic force constants from first principles calculations. *Phys. Rev. B* **2008**, *77*, 144112.
- (47) Zhou, F.; Nielson, W.; Xia, Y.; Ozoliņš, V.; others Compressive sensing lattice dynamics. I. General formalism. *Phys. Rev. B* **2019**, *100*, 184308.
- (48) Zhou, F.; Sadigh, B.; Åberg, D.; Xia, Y.; Ozoliņš, V.; others Compressive sensing lattice dynamics. II. Efficient phonon calculations and long-range interactions. *Phys. Rev. B* **2019**, *100*, 184309.
- (49) Tadano, T.; Tsuneyuki, S. First-principles lattice dynamics method for strongly anharmonic crystals. *J. Phys. Soc. Jpn.* **2018**, *87*, 041015.
- (50) Errea, I.; Rousseau, B.; Bergara, A. Anharmonic stabilization of the high-pressure simple cubic phase of calcium. *Phys. Rev. Lett.* **2011**, *106*, 165501.
- (51) Li, W.; Carrete, J.; Katcho, N. A.; Mingo, N. ShengBTE: A solver of the Boltzmann transport equation for phonons. *Comput. Phys. Commun.* **2014**, *185*, 1747–1758.

- (52) Han, Z.; Yang, X.; Li, W.; Feng, T.; Ruan, X. FourPhonon: An extension module to Sheng-BTE for computing four-phonon scattering rates and thermal conductivity. *Comput. Phys. Commun.* **2022**, *270*, 108179.
- (53) Ganose, A. M.; Park, J.; Faghaninia, A.; Woods-Robinson, R.; Persson, K. A.; Jain, A. Efficient calculation of carrier scattering rates from first principles. *Nat. Commun.* **2021**, *12*, 2222.
- (54) Claes, R.; Brunin, G.; Giantomassi, M.; Rignanese, G.-M.; Hautier, G. Assessing the quality of relaxation-time approximations with fully automated computations of phonon-limited mobilities. *Phys. Rev. B* **2022**, *106*, 094302.
- (55) Johnson, E. R.; Keinan, S.; Mori-Sánchez, P.; Contreras-García, J.; Cohen, A. J.; Yang, W. Revealing noncovalent interactions. *J. Am. Chem. Soc.* **2010**, *132*, 6498–6506.
- (56) Lu, T.; Chen, Q. Interaction region indicator: a simple real space function clearly revealing both chemical bonds and weak interactions. *Chemistry-Methods* **2021**, *1*, 231–239.
- (57) Jaffe, J.; Zunger, A. Theory of the band-gap anomaly in ABC₂ chalcopyrite semiconductors. *Phys. Rev. B* **1984**, *29*, 1882.
- (58) Jaffe, J.; Zunger, A. Anion displacements and the band-gap anomaly in ternary ABC₂ chalcopyrite semiconductors. *Phys. Rev. B* **1983**, *27*, 5176.
- (59) Gholami, M.; Hajiahmadi, Z.; Naghavi, S. S. Unlocking the potential of coinage-based quaternary chalcogenides for thermoelectricity. *J. Mater. Chem. A* **2024**,
- (60) Christensen, M.; Abrahamsen, A. B.; Christensen, N. B.; Juranyi, F.; Andersen, N. H.; Lefmann, K.; Andreasson, J.; Bahl, C. R.; Iversen, B. B. Avoided crossing of rattler modes in thermoelectric materials. *Nat. Mater.* **2008**, *7*, 811–815.
- (61) Li, W.; Carrete, J.; Madsen, G. K.; Mingo, N. Influence of the optical-acoustic phonon hybridization on phonon scattering and thermal conductivity. *Phys. Rev. B* **2016**, *93*, 205203.

- (62) Li, J.; Wei, L.; Ti, Z.; Ma, L.; Yan, Y.; Zhang, G.; Liu, P.-F. Wavelike tunneling of phonons dominates glassy thermal conductivity in crystalline $\text{Cs}_3\text{Bi}_2\text{I}_6\text{Cl}_3$. *Phys. Rev. B* **2023**, *108*, 224302.
- (63) Zeng, Z.; Zhang, C.; Ouyang, N.; Chen, Y. Extreme in-plane phonon blocking in simple chainlike crystals. *Phys. Rev. B* **2022**, *106*, 054302.
- (64) Ravichandran, N. K.; Broido, D. Phonon-phonon interactions in strongly bonded solids: selection rules and higher-order processes. *Phys. Rev. X* **2020**, *10*, 021063.
- (65) Zhu, Y.; Xia, Y.; Wang, Y.; Sheng, Y.; Yang, J.; Fu, C.; Li, A.; Zhu, T.; Luo, J.; Wolverton, C.; others Violation of the T^{-1} relationship in the lattice thermal conductivity of Mg_3Sb_2 with locally asymmetric vibrations. *Research* **2020**,
- (66) Pei, Y.; Shi, X.; LaLonde, A.; Wang, H.; Chen, L.; Snyder, G. J. Convergence of electronic bands for high performance bulk thermoelectrics. *Nature* **2011**, *473*, 66–69.
- (67) Tang, Y.; Gibbs, Z. M.; Agapito, L. A.; Li, G.; Kim, H.-S.; Nardelli, M. B.; Curtarolo, S.; Snyder, G. J. Convergence of multi-valley bands as the electronic origin of high thermoelectric performance in CoSb_3 skutterudites. *Nat. Mater.* **2015**, *14*, 1223–1228.
- (68) Brlec, K.; Spooner, K. B.; Skelton, J. M.; Scanlon, D. O. $\text{Y}_2\text{Ti}_2\text{O}_5\text{S}_2$ —a promising n-type oxysulphide for thermoelectric applications. *J. Mater. Chem. A* **2022**, *10*, 16813–16824.
- (69) Wei, S.-H.; Zunger, A. Calculated natural band offsets of all II–VI and III–V semiconductors: Chemical trends and the role of cation d orbitals. *Appl. Phys. Lett.* **1998**, *72*, 2011–2013.
- (70) Ghorbani, E. On efficiency of earth-abundant chalcogenide photovoltaic materials buffered with CdS: the limiting effect of band alignment. *Journal of Physics: Energy* **2020**, *2*, 025002.
- (71) Lavasani, A.; Bulmash, D.; Sarma, S. D. Wiedemann-Franz law and Fermi liquids. *Phys. Rev. B* **2019**, *99*, 085104.

- (72) Madsen, G. K.; Carrete, J.; Verstraete, M. J. BoltzTraP2, a program for interpolating band structures and calculating semi-classical transport coefficients. *Comput. Phys. Commun.* **2018**, *231*, 140–145.

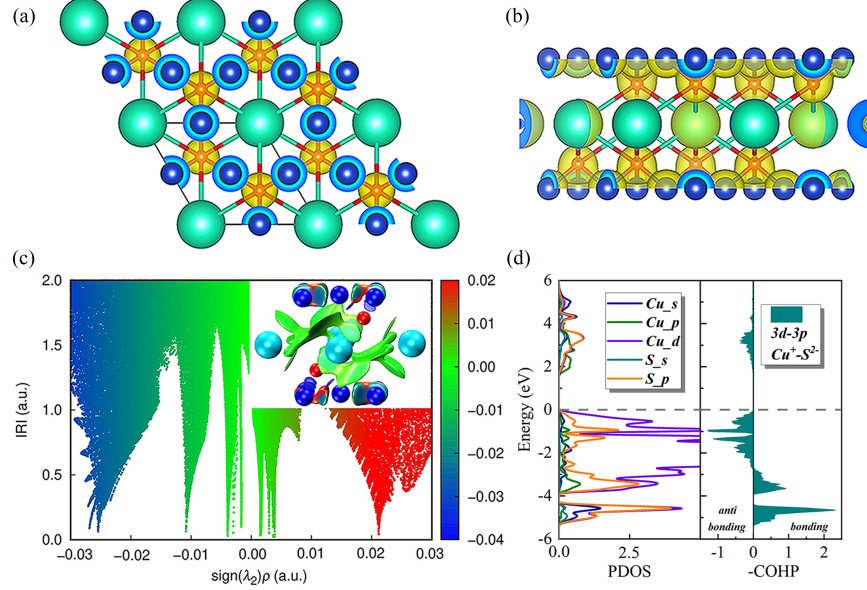


Figure 1: Structure configurations coupled with charge distribution form the (a) in-plane and (b) out-of-plane perspectives. The cyan, blue, and red spheres denote cesium, copper, and sulfur atoms, respectively. (c) Non-covalent interaction analysis associated with interaction region indicator (IRI). Inset: Isosurface map with standard coloring method and chemical explanation of $\text{sign}(\lambda_2)\rho$ on IRI isosurfaces. (d) Orbital-resolved projected density of states (PDOS) and crystal orbital Hamilton populations (COHP) of the $\text{Cu}^+-\text{S}^{2-}$ orbital interaction.

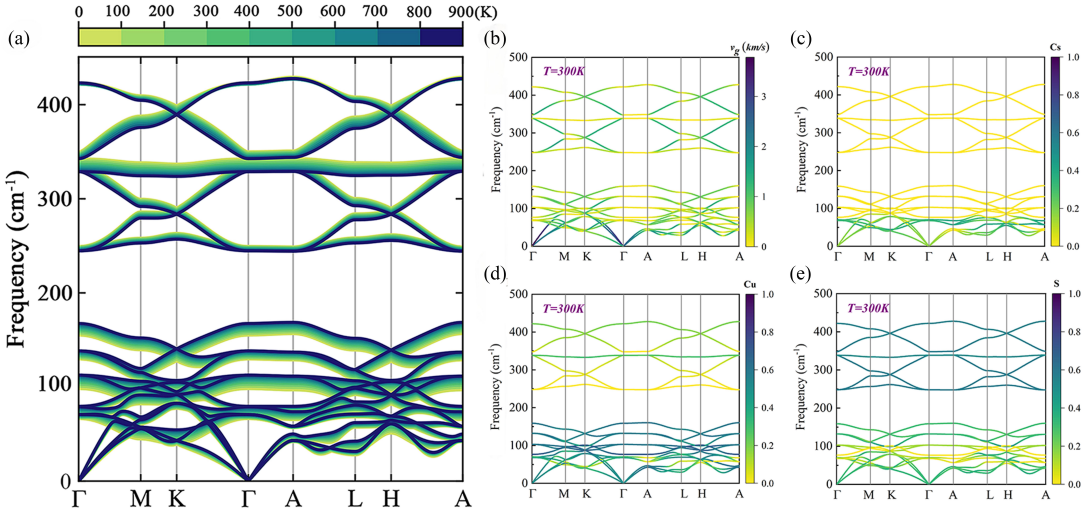


Figure 2: (a) Anharmonically renormalized phonon dispersions at finite temperatures in comparison with harmonic approximation (HA). (b) Phonon group velocity projection onto the phonon dispersions at 300 K. (c) Color-coded atomic participation ratio (APR) of Cs atoms projected onto the phonon dispersions at 300 K. (d) The same as (c) but for Cu atoms. (e) The same as (c) but for S atoms.

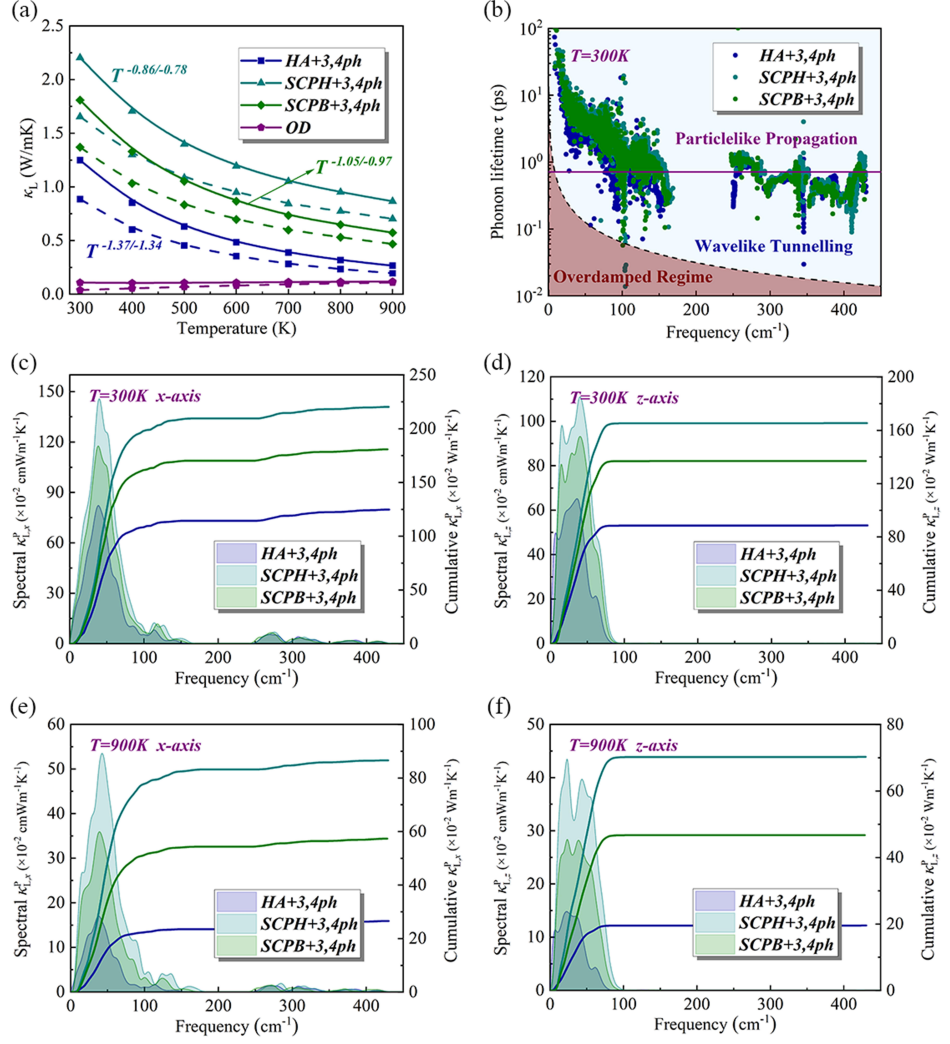


Figure 3: (a) Temperature-dependence of lattice thermal conductivity using various theories including HA+3/4ph, SCPH+3/4ph, SCPB+3/4ph, and OD model. The solid and dotted lines correspond to the x and z directions, respectively. (b) Calculated phonon lifetime as a function of frequency at 300 K, where the black dotted line and red solid line represent the Ioffe-Regel limit and Wigner limit in time. (c) Calculated spectral/cumulative populations' thermal conductivity along the x -axis at 300 K. (d) The same as (c) but for z -axis. (e) The same as (c) but for 900 K. (f) The same as (d) but for 900 K.

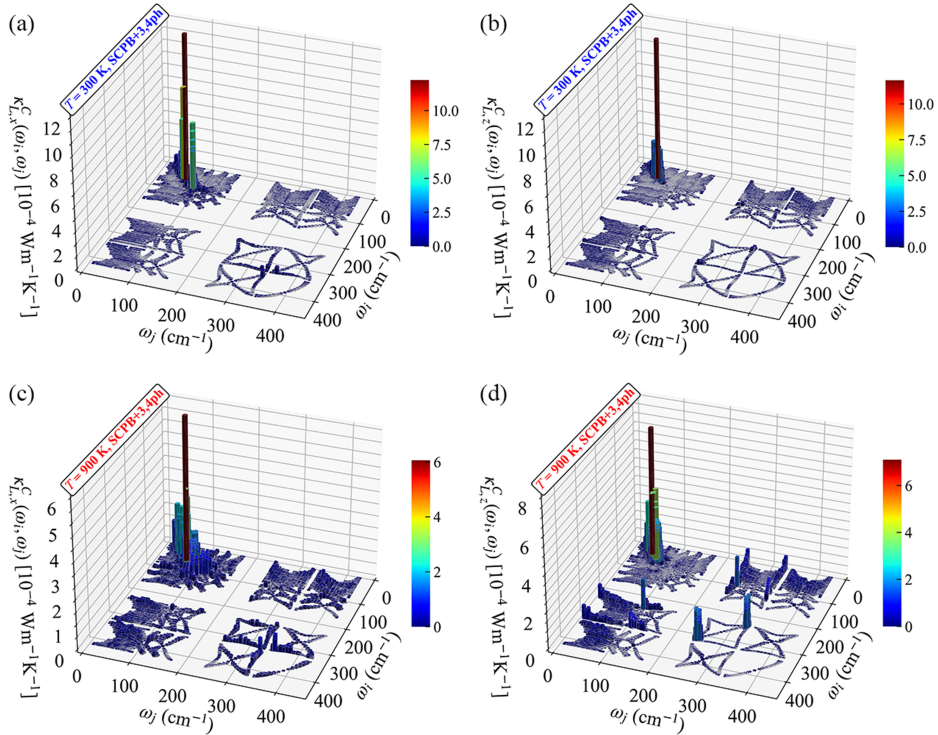


Figure 4: (a) Three-dimensional visualizations $\kappa_{L,x}^C(\omega_{qj}, \omega_{qj'})$ of the coherences' thermal conductivity based on the SCPB+3,4ph model along with the x -axis at 300 K. The diagonal data points ($\omega_{qj} = \omega_{qj'}$) indicate phonon degenerate eigenstates. (b) The same as (a), but for z -axis. (c) The same as (a), but for 800 K. (d) The same as (b), but for 800 K.

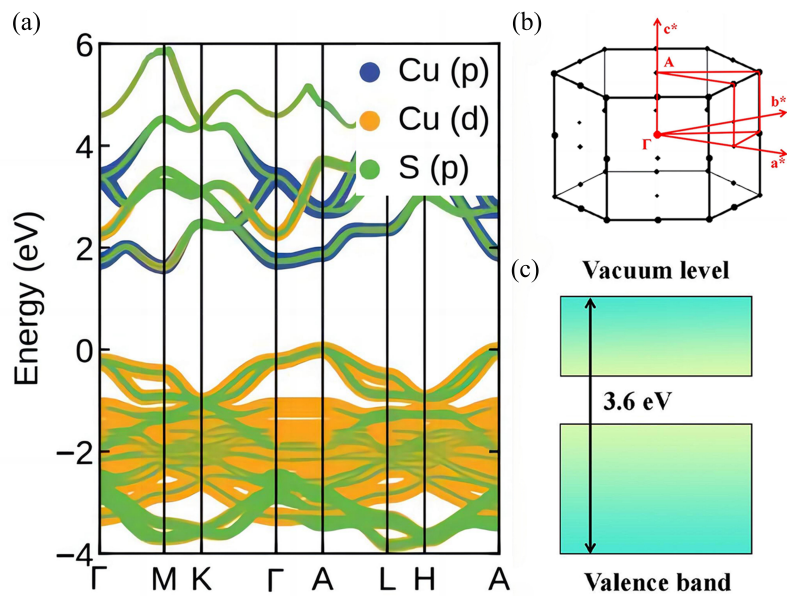


Figure 5: (a) Atom-projected electronic band structures for CsCu_3S_2 . The blue, orange, and green projections represent the contributions of the $\text{Cu}(p)$, $\text{Cu}(d)$, and $\text{S}(p)$ orbitals, respectively. (b) First Brillouin zone and high-symmetry k -path of CsCu_3S_2 . (c) Band alignment for CsCu_3S_2 with energies calculated relative to the Cu $2p$ state.

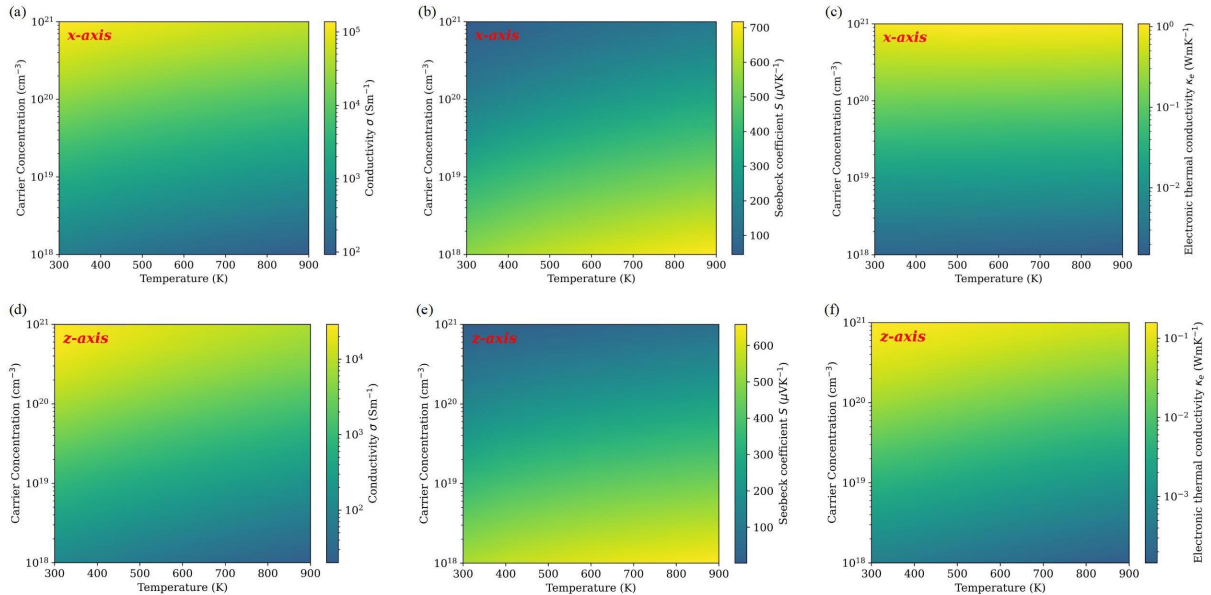


Figure 6: Calculated *p*-type electronic transport properties including the (a) conductivity σ , (b) Seebeck coefficient S , and (c) electrical thermal conductivity κ_e along with the *x*-axis, corresponding to carrier concentrations ranging from 10^{18} to 10^{21} cm^{-3} and temperatures from 300 to 900 K. (d) The same as (a), but for *z*-axis. (e) The same as (b), but for *z*-axis. (f) The same as (c), but for *z*-axis.

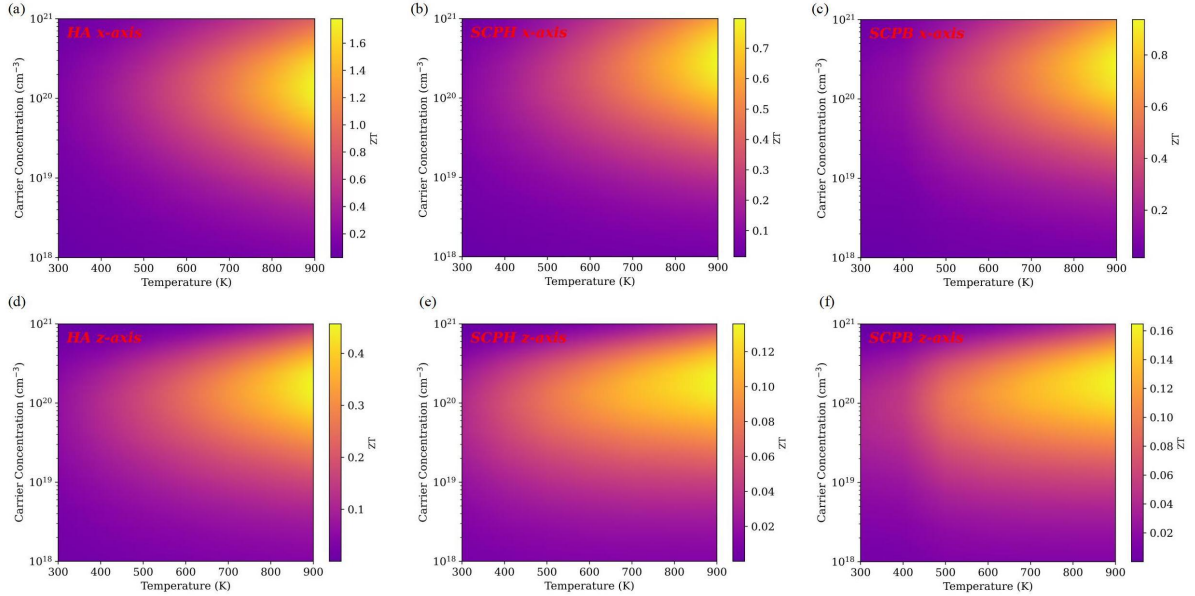


Figure 7: Calculated *p*-type thermoelectric figure of merit ZT along with the x -axis, based on the (a) HA, (b) SCPH, and (c) SCPB+OD model, respectively, corresponding to carrier concentrations ranging from 10^{18} to 10^{21} cm^{-3} and temperatures spanning from 300 to 900 K. (d) The same as (a), but for z -axis. (e) The same as (b), but for z -axis. (f) The same as (c), but for z -axis.